

DYNAMIC RECONFIGURABLE PATH PLANNING FOR FIRE-FIGHTING UAVS

Zegong Lin[1], David Geraghty[1], Sophie F. Armanini[1] & Laura Mainini[1,2]

[1]Imperial College London, Department of Aeronautics, SW7 2AZ, London, UK
[2]Imperial College London, Brahmal Vasudevan Institute of Sustainable Aviation, SW7 2AZ, London, UK

Abstract

We present a dynamic reconfigurable mission planning framework for wildfire monitoring tasks using unmanned aerial vehicles (UAVs). The framework integrates real-time temperature field sensing, an information value model based on fireground proximity, and a thermal damage probability model that penalises exposure to high temperatures, ensuring the feasibility of the task path and flight safety. At the mission level, the UAV can dynamically switch between states such as search, tracking, and escape. At the path level, an information-driven planner based on local perception can adjust the flight trajectory in real time when the environment is partially observable. Simulation results show that the proposed adaptive framework substantially increases mission completion rate, information acquisition efficiency, and UAV survivability compared to traditional pre-planning strategies in dynamic disaster scenarios such as wildfires. The research findings indicate that combining data-driven objectives with thermal risk management enhances the adaptability and mission completion rate of UAVs in dynamic disaster environments.

Keywords: UAVs, mission planning, wildfire monitoring, adaptive/dynamic planning

1. Introduction

Unmanned aerial vehicles (UAVs) demonstrate significant potential for disaster monitoring missions. However, such missions usually take place in hazardous dynamic environments and involve changing mission objectives and dynamic mission objectives and complex environments with multiple operational constraints pose a major challenge to UAVs. In applications such as wildfire monitoring, for instance, rapidly changing fire locations and temperature distributions present difficulties for traditional mission planning approaches [1]. To enable UAVs to perform complex missions in dynamic environments, reconfigurable mission planning approaches are needed, which integrate real-time sensing and adaptive path replanning, enabling UAVs to adjust their objectives and path during a mission, improving the chances of mission success [2].

Mission planning for aerial vehicles typically follows a layered architecture, where a mission manager issues high-level objectives and a path planner generates feasible trajectories under given constraints. Reconfigurable mission plans enable restructuring in response to changing conditions. Prior work has for instance proposed the use of mission graphs and runtime cost evaluation [3], partially observable Markov decision process formulations for decision-making under uncertainty [4], or capability-based replanning, where future intentions are replanned when they would breach the limits of the real-time flight envelope estimate [5]. Health and risk considerations can be integrated into mission planning to ensure safety, e.g. via battery health-aware task verification [6]. At the lower level, dynamic environments also require path planning methods to be adaptable or robust to unforeseen changes. Data-driven methods such as deep reinforcement learning have been explored for dynamic path planning, however the high flexibility they achieve comes at a high computational cost [7]. In dynamic monitoring misisons, UAV objectives extend beyond navigation to encompass information

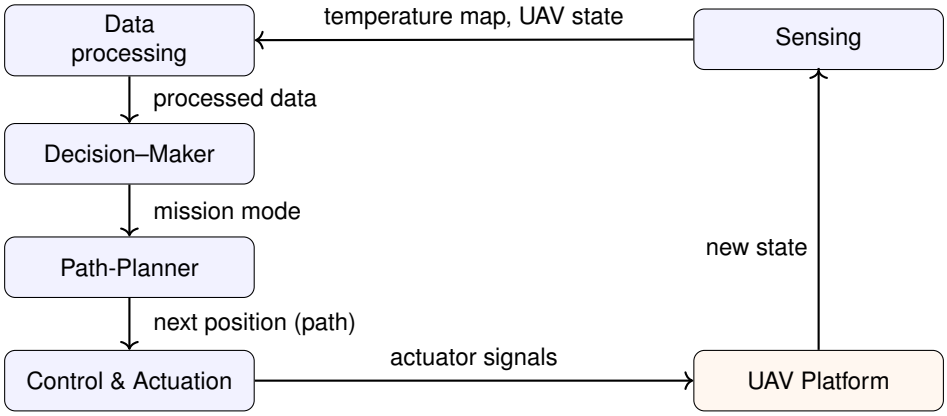


Figure 1 – Schematic of the system's core data flow and reconfiguration loop

acquisition. Information-driven path planning models support adaptive monitoring in complex environments [8], guiding UAVs toward regions of high uncertainty, i.e. information gain.
Despite significant progress in UAV mission planning, most work focuses on single aspects, e.g. path planning or health modelling, without integrating these capabilities into a single real-time decision-making framework. Most existing path planning methods focus on trajectory feasibility or optimisation, with limited consideration of high-level mission adaptability. Mission reconfiguration is mostly considered at a conceptual level [3] and rarely coupled with online path planning, thus constraining UAV responsiveness in dynamic or uncertain environments. Likewise, information-based planning approaches [9, 8] and health and risk models [6] are typically explored separately. A multi-objective, multi-constraint framework that jointly optimises information acquisition, system health and mission risk in real time is still lacking, and would be invaluable for autonomous UAV operations in uncertain dynamic environments.
In this paper, we present a reconfiguration-capable mission planning framework, which enables UAVs to dynamically adjust their planning strategies in response to real-time changes in environment or mission requirements. The framework integrates a mission-level decision system with a local path planning algorithm, ensuring that the UAV achieves its mission objectives while maintaining operational safety. We demonstrate its usage for wildfire monitoring, including the full cycle of fire detection, tracking and area withdrawal, based on real-time fire conditions. Our framework aims to enhance UAV mission adaptability and robustness in dynamic environments, while maximising information acquisition efficiency and reducing the risk of UAV damage. To test our framework in different wildfire scenarios, we constructed a simplified wildfire simulation environment. Results show that the framework enables UAVs to autonomously adjust their flight path and mission modes in response to real-time changes in the environment or the UAVs own health state. This leads to higher success rates for UAVs conducting monitoring tasks in uncertain environments such as wildfires.

2. Methodology and System Architecture

The proposed reconfigurable mission planning system, shown in Fig. 1, consists of four core components: sensing; data processing; decision and task recognition; and path planning. The UAV first acquires environmental and self-state information, which is then processed into performance constraints and mission features. These features are subsequently analysed by the decision module to identify the task state. Finally, an optimal path is generated and executed under the specified constraints. An overview of each of the listed components is given in the subsequent subsections.

2.1 Sensing module

The on-board **sensing module** collects environmental and self-state data in real time, enabling the system to detect changes during flight, and providing essential data for subsequent planning. Sensors considered inlude basic flight sensors, providing UAV position and velocity, and payload sensors, such as temperature sensors and cameras, which perceive changes in the external environmental conditions. As our purpose is to demonstrate the effectiveness of the high-level concept, we assume

that the sensors are ideal and can instantly provide preprocessed valid data. A simplified sensor health status is defined, which divides sensors into "normal" and "faulty" categories.

2.2 Data processing module

The **data processing module** processes the sensor data to extract relevant information on the UAV's health and performance, which will subsequently be used for mission planning. Given the focus on wildfire monitoring, this module specifically considers the effect of fire-related changes in the environment. Temperature is a critical factor in this context, influencing the UAV's structural and aerodynamic performance, flight power requirements, battery performance and sensor reliability. Hence, the effects of temperature on key subsystems were modelled.

2.2.1 Propulsion Performance

The effect of temperature on propulsion performance was captured in terms of the extra thrust and power requirements resulting from lower air density at higher temperatures, assuming steady level flight conditions. Lift and drag both depend on air density, via the well-known expressions:

$$L = \frac{1}{2}\rho V^2 S C_L, \quad D = \frac{1}{2}\rho V^2 S C_D, \tag{1}$$

where C_L and C_D are the lift and drag coefficients, ρ is air density, V is velocity and S is wing area. Moreover, the lift and drag coefficients are coupled via the induced drag C_{Di}:

$$C_D = C_{D0} + C_{Di} = C_{D0} + kC_L^2 \tag{2}$$

where C_{D0} is the zero-lift drag coefficient and k is a constant. In steady level flight, lift must be equal to weight, and thrust to drag. To maintain an equilibrium when air density decreases, the angle of attack must be increased to increase the lift coefficient. This in turn will increase the induced drag and hence the total drag[1] A higher drag will lead to a higher thrust requirement, according to:

$$T_{req} \stackrel{!}{=} D = \frac{1}{2}\rho V^2 S C_D. \tag{3}$$

The corresponding power likewise depends on the thrust (i.e. the drag):

$$P = T \cdot V = D \cdot V. \tag{4}$$

In summary, an increase in ambient temperature implies a decrease in air density, which leads to an increase in thrust demand and power consumption.

2.3 Battery Performance

The UAV was assumed to be powered by a battery pack. During flight, the battery experiences a high discharge rate and temperature rise, making it the most critical component in terms of thermal safety. Given the propulsion power P obtained in eq. 4, the discharge current can be computed as:

$$I = \frac{P}{U} \tag{5}$$

where U is the battery voltage. This current serves as input for the battery thermal model.
A lumped thermal model [10] was used to compute the total heat generated:

$$Q = I(U_c - \alpha U_a - U - T\frac{dU}{dT}) \tag{6}$$

where U_c is the cathode voltage, U_a is the anode voltage, scaled by a factor α (related to electrode geometry and capacity loading of cathode / anode in a given battery), $\frac{dU}{dT}$ is the temperature coefficient, and T is the current battery temperature. The first term in the equation represents the electrochemical heat associated with the current flow, while the subsequent terms capture the temperature-dependence of the open-circuit voltage. The evolution of the battery temperature is then described by:

$$\frac{\partial T}{\partial t} = \frac{Q}{m_{cell} C_p} - \eta_{conv}(T - T_{amb}) \tag{7}$$

[1] Note that the increase in induced drag dominates over the direct effect of lower air density on produced drag force.

where m_{cell} is the battery cell mass, C_p is the specific heat capacity, and η_{conv} is the convective coefficient, defined as:

$$\eta_{conv} = \frac{A_{surf}}{C_p m_{cell}} h_{conv} \tag{8}$$

where A_{surf} is the surface area of the cell, and h_{conv} is the convective heat transfer coefficient. The first term reflects the accumulation of internal heat within the cell, while the second term represents convective heat dissipation between the battery and the environment.
To estimate the state-of-charge (SOC) in real time, the Coulomb counting method was used. At each time step, the remaining capacity C_{remain} (in Ah) is updated by integrating the discharge current:

$$C_{remain}(t) = C_{remain}(t - \Delta t) - \frac{I(t)\Delta t}{3600} \tag{9}$$

The SOC is then calculated as the ratio of remaining capacity to nominal capacity C_{max}:

$$SOC_t = \frac{C_{remain}(t)}{C_{max}} \tag{10}$$

The above model can be used to estimate battery temperature and remaining capacity in real time, providing inputs for the mission planning module.

2.3.1 Sensor Damage

Due to prolonged exposure to high temperatures, the onboard sensors accumulate thermal stress. Their failure probability increases with exposure temperature and time. To capture this process, a probabilistic model based on a Poisson distribution was formulated to estimate sensor failure risk.
A temperature-dependent failure rate $\lambda(T)$ was defined. When the sensor is exposed to temperatures above the safe threshold T_{safe}, the failure rate grows nonlinearly with temperature. At or below this threshold, only a background failure rate is assumed:

$$\lambda(T) = \begin{cases} \lambda_0 (T - T_{safe})^p, & T > T_{safe} \\ \lambda_{cold}, & T \leq T_{safe} \end{cases} \tag{11}$$

The cumulative hazard over time is then expressed as:

$$H(t) = \int_0^t \lambda(\tau) d\tau \tag{12}$$

The cumulative failure probability is obtained using the Poisson cumulative distribution:

$$P_{fail}(t) = 1 - e^{H(t)} \tag{13}$$

To simulate realistic failure events, a Monte Carlo fault injection approach was used. In each round of simulations, a random number $r \in [\theta, 1)$ was generated. If $r < P_{fail}(t)$, the sensor was marked as failed. The threshold θ was used to avoid random trigger values close to 0, which could cause false-positive failures. This approach allows the sensor health status to be dynamically reflected in the mission planning, enabling the system to replan missions after a failure.

2.4 Decision-making module

Using the measured and calculated data, the **decision-making module** continually assesses the UAV's operational status in real time and determines the appropriate mission mode (search, track, escape), based on predefined rules integrating reactive and predictive mechanisms. These high-level behavioural instructions represent execution objectives for the path-planning module. When the environment or mission objectives change, the decision module triggers a mission reconfiguration. Its key function is thus to convert continuous data from the lower-level perception layer into discrete decisions at the higher levels, providing execution objectives for the path planning module.
The decision module is a finite-state machine (FSM) (cf. fig. 2), which switches between mission modes based on internal UAV states and external environmental factors. The continual asessment of the current situation considers two types of states:

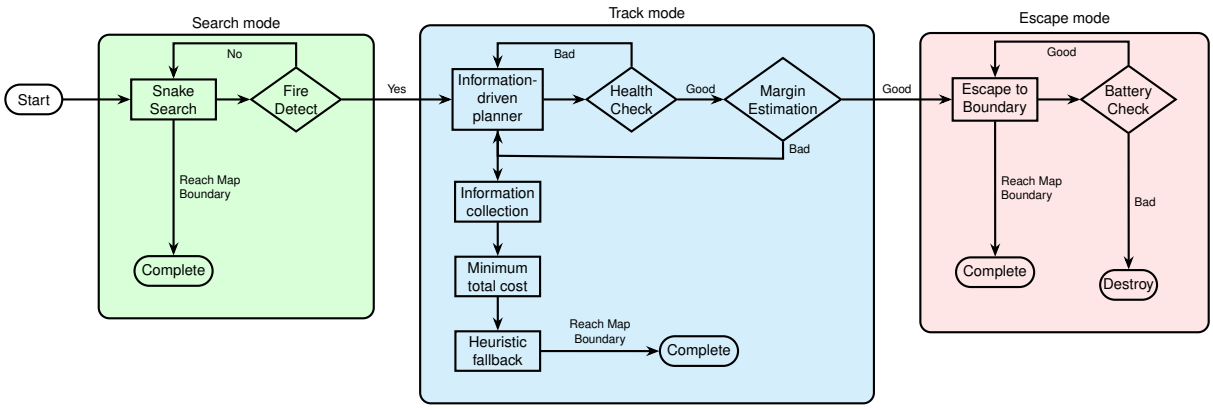


Figure 2 – Flow diagram of decision-making finite-state machine.

1. The **mission target state** determines whether a target to be tracked (e.g. a fire point) has been detected within sensing range, and if so, triggers a transition from 'search' to 'track' mode.

2. The **system viability state** assesses whether the UAV is able to safely continue executing its current mission by considering the following metrics:

   - *Battery thermal state*. This state is based on a comparison between the current battery temperature T_{batt} and pre-defined thresholds. Soft threshold T_{soft} triggers a performance degradation warning, hard threshold T_{hard} triggers the escape mode, and critical threshold T_{crit} represents battery thermal runaway, assumed to lead to mission failure.
   - *State of charge (SOC)*. When $SOC < SOC_{min}$, energy is about to be depleted.
   - *Sensor health state*. Based on the cumulative damage model discussed in section 2.3.1, when the cumulative damage value exceeds the random reliability threshold, the sensor is assumed to have failed.
   - *Predictive sustainability state*. This state compares the predicted mission completion time $t_{complete}$ with the estimated maximum sustainable operation time $t_{sustain}$, considering current energy consumption and thermal load. $t_{sustain}$ is defined as the smaller value between battery thermal failure time and battery depletion time. A dynamic safety margin coefficient α is defined, related to the mission depth, to construct a predictive risk indicator.

The above evaluations trigger state transitions in the FSM between the following modes:

1. **Search Mode**: the UAV conducts a large-scale search of the task area. If a target is identified, it transitions to track mode.

2. **Track Mode**: the UAV collects data on the identified targets, while performing the following types of monitoring and/or reconfiguration:

   (a) Reactive: if any system-critical parameter exceeds its hard safety threshold, transition to escape mode is triggered.

   (b) Predictive: if predictive risk indicators suggest that the time required for mission completion will exceed the maximum sustainable time, an escape is triggered.

3. **Escape Mode**: the UAV attempts to escape to a safe area in the most direct way possible.

The FSM passes a set of high-level behavioural instructions to the path planner (sec. 2.5), which uses them to generate flight paths. By continuously monitoring system and environment, and combining real-time responses with predictions, the decision-making system achieves autonomous, safe behaviour mode switching in uncertain environments, enabling mission reconfigurability.

2.5 Path-planning module

Finally, the **path planning module** receives instructions (search, track, escape) from the decision module, and uses these to generate safe and executable flight paths. Three distinct approaches are used to generate paths, maximising, respectively, area coverage, information, and survival probability.

2.5.1 Search Mode: Global Coverage Planning

In **search mode**, the path-planner aims to achieve efficient global coverage to maximise the probability of discovering potential points of interest (e.g., in our example, fire sources). The current system uses a lawnmower pattern path, which consists of a predefined back-and-forth movement pattern, as shown subsequently in Fig. 6a. In our implementation, the planner starts at the top-left corner of the mission area [0,0], with a motion along the positive X-axis. The path planned by this method has an extremely low computational overhead, and in a static environment, it guarantees 100% coverage of the defined area. Once started, this mode continues to run until the sensors detect a target and report this back to the decision module. At this point, depending on the specific event, either a switch to tracking mode is triggered, or the search mode is maintained. If no mode switches are triggered, the mission proceeds until the UAV reaches the end of the map (bottom right corner).

2.5.2 Track Mode: Local Multi-Objective Optimization Planning

In **track mode**, the aim is to maximise information collection efficiency while ensuring the UAV's safety. Path planning is based on a local multi-objective optimisation, based on model predictive control (MPC). By defining a cost function that integrates information value, thermal risk and safety constraints within a limited preview field of view, intelligent navigation in dynamic and hazardous environments is enabled. The path planning is a local multi-objective optimisation, based on model-predictive control, and can be expressed as a rolling optimisation problem in a finite time domain. At each planning cycle, an optimisation problem is solved based on the current state to determine the optimal control input sequence. To reduce computational complexity, the preview window is set to $N = 1$, which corresponds to single-step forward optimisation.

$$u_k^* = \arg\min_{u \in U} L(x_k, u) \tag{14}$$

Where U is the feasible control set corresponding to the 8-connected neighbourhood points on the grid map used.
The multi-objective cost function L consists of five terms.

$$\begin{aligned} L_{total}(p) &= L_{info} + L_{mem} + L_{risk} + L_{high-T} + L_{smooth} \\ &= -\mu I(p) + \omega V(p) + \beta R(p) + L_{high-T}(p) + \kappa(1 - \cos\theta) \end{aligned} \tag{15}$$

where μ, β, ω and κ are weighting factors.
L_{info} encourages the UAV to access areas with high information gain, e.g. the fire line. An information value map $I(p)$ is constructed by superimposing a Gaussian kernel function on each edge point p, obtained using the Sobel operator. The information value map is weighted by a factor $\mu_{info}A$ and flows negatively into the cost function.

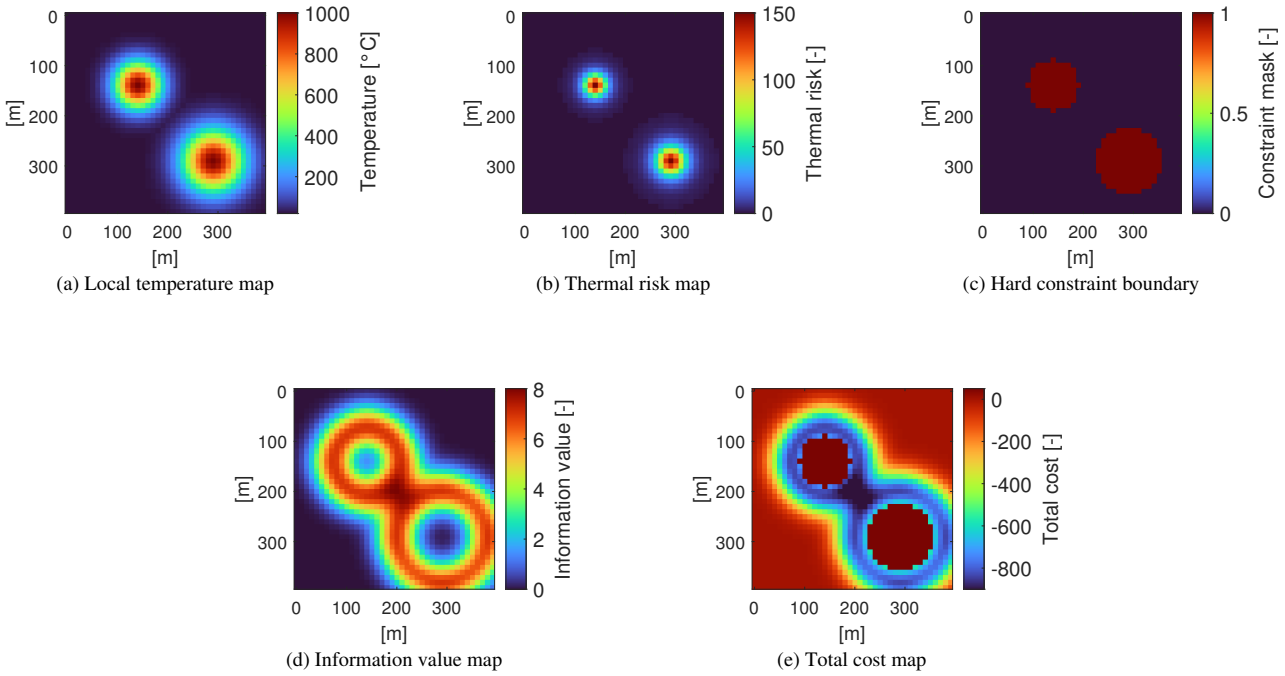
$$L_{info} = -\mu_{info} I(p), \quad I(p) = \sum_{k=1}^{N_{edge}} A \exp\left(-\frac{||p - p_k||^2}{2\sigma^2}\right) \tag{16}$$

The fire area mask M_{fire} is obtained by thresholding the temperature.

$$M_{fire}(p) = \begin{cases} 1, & T(p) > T_{fire} \\ 0, & otherwise \end{cases} \tag{17}$$

L_{mem} encourages exploration by penalising a return to visited areas, based on a visitation graph $V(p)$ that records the number of visits to each location:

$$L_{mem} = \omega \cdot V(p) \tag{18}$$



(a) Local temperature map (b) Thermal risk map (c) Hard constraint boundary

(d) Information value map (e) Total cost map

Figure 3 – Visualisation of local cost function composition.

L_{risk} promotes thermal risk avoidance, and is a function of the risk of equipment damage R, modelled as an exponential function of temperature. This results in the following cost function term:

$$L_{risk} = \beta R(p), \quad \text{where} \quad R(p) = \begin{cases} \exp\left(\lambda_{dmg}(T(p) - T_{fire})\right), & T(p) > T_{fire}, \\ 0, \quad \text{otherwise} \end{cases} \tag{19}$$

L_{high-T} assigns an infinite cost to areas where the temperature exceeds the absolute threshold $(T(p) \geq T_{hard})$.

$$L_{high-T}(p) = \infty, \quad \text{if} \quad T(p) \geq T_{hard} \tag{20}$$

Finally, L_{smooth} ensures motion smoothness by suppressing large-angle manoeuvres, and is a function of the angle θ between the candidate direction and the previous direction.

$$L_{smooth} = \kappa(1 - \cos\theta) \tag{21}$$

where θ is the angle between the candidate direction and the previous direction.
During solution, the planner selects as next position the neighbouring point with the lowest cost.

$$p = \arg\min_{p \in N_8} L_{total}(p) \tag{22}$$

If all neighbouring points violate the constraints, the feasible point with the lowest temperature is chosen as next position.
Figure 3 provides a visual representation of how the local cost function is constructed, for an arbitrary example with two fire sources. As highlighted by the figure, the cost function is essentially a trade-off between maintaining safety and maximising information gain. In the final cost map, a low-cost area along the fire line region can be seen, where the UAV would choose to fly.

2.5.3 Escape Mode: Shortest Path Planning

When **escape mode** is triggered, all other tasks are interrupted to focus on the UAV's survival. The path planner aims to minimise the time needed to leave the danger zone. Minimum time is given by,

$$t_{escape} = \frac{L(p_{start}, p_{exit})}{v}, \tag{23}$$

where L is the distance from the current position to the exit location, and v is the airspeed of the UAV.

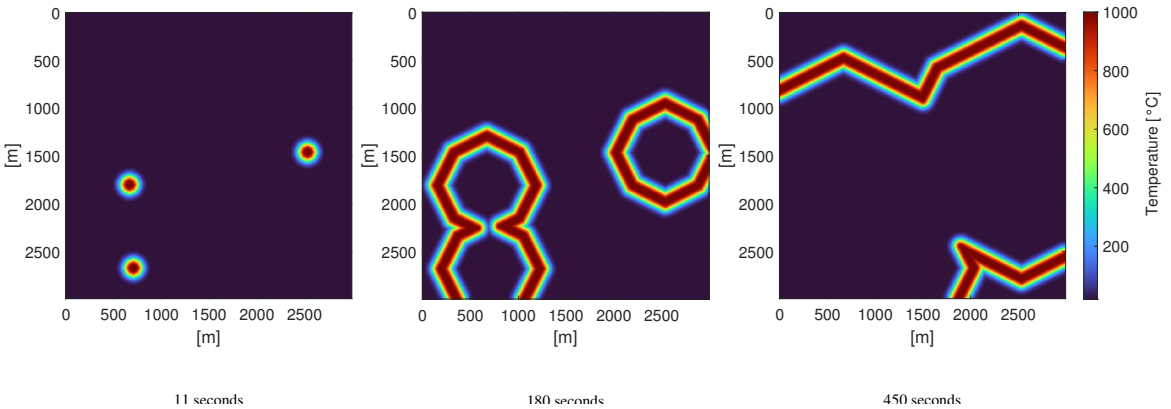


Figure 4 – Fire temperature maps for the case of 3 random fire sources

The planner first calculates the straight-line distance from the current position to the map boundaries and selects the nearest boundary point as exit. Then, a steepest descent method is used to generate a path to the map boundary point closest to the UAV. At each step, the neighbouring gridpoint that most reduces the distance to the exit is chosen as next waypoint. The escape mode has maximum priority and cannot be deactivated once triggered. The path points generated by the path planning module are transmitted to the flight control system.

2.6 Reconfigurable Mission Planning

The framework's **reconfigurable mission planning** capability is achieved by a highly modular, data-driven distributed architecture, which integrates the discussed components via continuously running dataflows. The perception module continually collects information on the fire situation, while at the same time the UAV's internal diagnostic program generates system status monitoring datastreams. The decision-maker considers both datastreams and outputs instructions to the path planner, which converts them into executable sequences of path points. The framework thus enables UAVs to dynamically adjust their mission objectives and flight strategy to balance performance and safety in complex, uncertain environments, maximising mission success.

3. Simulation Setup

The proposed framework was evaluated through extensive simulations, using a fixed-wing UAV as a test platform. This section describes the simulation setup.

3.1 Aircraft Modelling

Table 2 lists the UAV and system parameters used in the simulations. The UAV's aerodynamic and battery parameters were based on existing studies [11, 12, 13], while sensor parameters were based on commercially available products (e.g., DJI ZENMUSE H30) and estimates [14]. The following assumptions were made to simplify the simulation process and facilitate initial evaluations:

- The UAV flies at a fixed low altitude in a 2D plane.
- The UAV maintains a constant cruising velocity throughout the mission.
- All turns are assumed to be perfectly coordinated and executed instantaneously.
- No wind or turbulence is considered.
- The UAV has perfect knowledge of its state (position, velocity, attitude) at all times.
- The onboard sensors provide instantaneous and error-free measurements.
- If a fault occurs, the UAV is assumed to have completed its current manoeuvre: replanning starts from the next waypoint.

Category	Parameter	Symbol	Value
Aircraft	Cruising speed	V	30 m/s
	Wing area	S	$1m^2$
	Zero-lift drag coefficient	C_{D0}	0.02
	Induced drag factor	k	0.045
	Lift coefficient	C_L	0.5
Battery Model	Full cell voltage	U_c	4.2 V
	Working voltage	U	3.7V
	Voltage offset	U_a	0.1 V/K
	Temperature coefficient	dU/dT	-0.001V/K
	Cell mass	m_{cell}	0.05kg
	Specific heat capacity	C_p	1200 $J/kg/K$
	Convection coefficient	h_{conv}	50 $W/m^2/K$
	Cell surface area	A_{surf}	$0.01m^2$
	Max capacity	C_{max}	6Ah
	Thermal threshold	T_{batt}	120$^\circ C$
	Critical temperature	T_{crit}	140$^\circ C$
Sensor Model	Operating temperature	T_{safe}	-20 to +50$^\circ C$
	Failure base rate	λ_0	0.01/3600 s^{-1}
	Cold failure rate	λ_{cold}	0.002/3600 s^{-1}
	Exponent factor	p	2
	Damage threshold	θ	0.01
Path Planner	Damage factor	λ_{dmg}	0.005
	Information weight	μ_{info}	120
	Damage penalty	β	0.05
	Memory decay	ω	1
	Angle penalty	κ	2.7
	Information collection radius	σ	300m

Table 1 – UAV, modelling and system parameters used for simulations.

3.2 Fire Modelling

A simplified 2D fire field model was constructed to simulate various wildfire scenarios, with different numbers of random fire sources. Fire points were randomly generated on a 300×300 point 2D-gridmap, with each initial fire point spanning one grid cell. The fire was assumed to spread radially at a constant speed, under a no-wind assumption [15]. Thus, unburned cells surrounding each burning cell were ignited at regular intervals. Burned cells were assumed to extinguish after a certain time, and cells burned once were assumed not to ignite again. When the fire line reached the map boundary, it was programmed to disappear. While wildfire-atmosphere interaction is a complex process, involving coupled combustion and fluid dynamics, simplified analytical kernels have been found to capture localised thermal effects adequately well. In particular, Gaussian radial basis functions have been successfully applied in 2D temperature reconstruction tasks [16], and Gaussian-shaped probability density functions are used in wildfire simulation frameworks such as FIRETEC to approximate sub-grid temperature statistics [17]. Thus, the local fire-induced heating field was approximated by a Gaussian distribution centred at each ignition point.
At each fire location (x_0, y_0), the temperature at a grid point (X,Y) can be expressed as:

$$T(X,Y) = T_a + (T_0 - T_a) \cdot \exp(-\frac{r^2}{2\sigma^2}) \tag{24}$$

where T_0 is the peak fire temperature, T_a the ambient temperature, r the radial distance from the fire centre, and σ the spread parameter. When r exceeds 3σ, the temperature field is truncated and the temperature assumed to return to ambient temperature. For multiple ignition points, the overall temperature field was computed as the maximum value of the overlapping contributions. Fig. 5 shows the temperature field evolution for the case of three random fire sources. Relevant parameters for the fire environment (fire spread rate, combustion and extinguishing times, flame temperature characteristics) were set based on existing fire dynamics research [18] and are reported in table 2

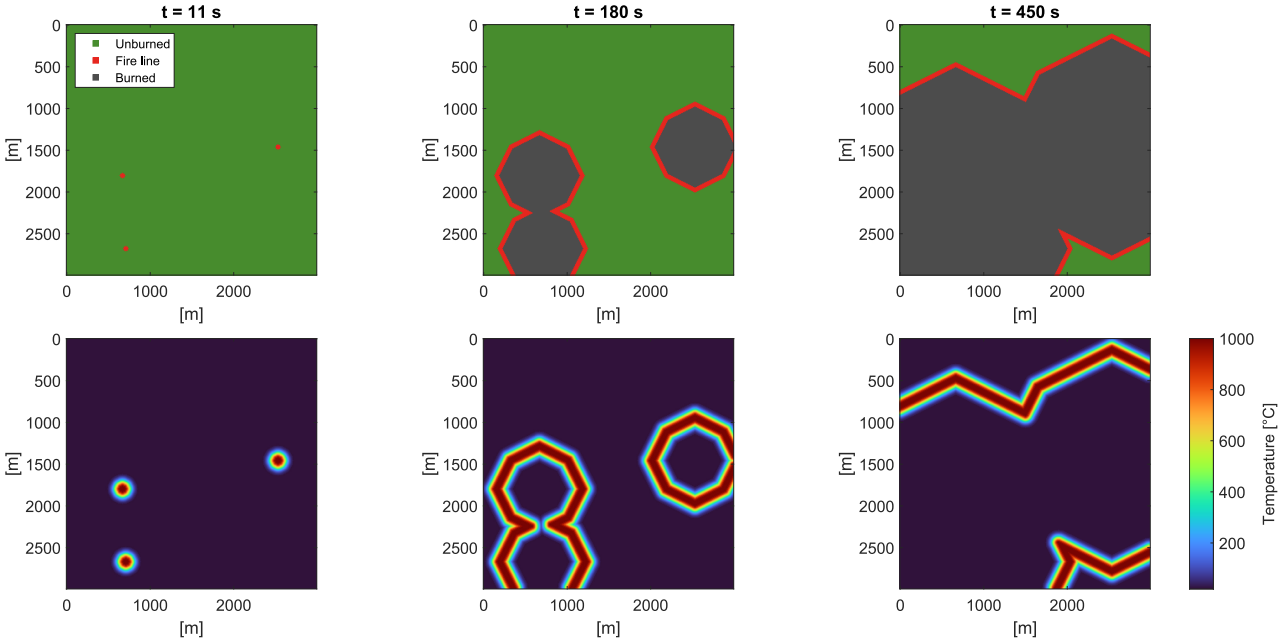


Figure 5 – Fire spread (top) and temperature (bottom) maps at three successive mission times (11s, 180s, 450s), for the case of three random fire sources.

Parameter	Symbol	Value
Sea-level pressure	P_0	101325 Pa
Gas constant	R	287.05 $J/kg/K$
1 Grid unit	-	10 m
Total map size	-	3000$m\times$ 3000m
Fire spread speed	-	1m/s
Burnout time	-	15s
Flame centre temperature	T_0	1000 $^\circ C$
Ambient temperature	T_a	20 $^\circ C$
Radial temperature decay	σ	5 gridpoints (50m)
Ignition radius	-	3 gridpoints (30m)

Table 2 – Simulation environment parameters

3.3 Monitoring and Margin Estimation

To allow for simulation of the framework, a mechanism of online monitoring, risk assessment and mode switching was implemented. In this context, the following simplifying assumptions were made:

- Battery capacity / temperature measurements and SOC estimates, are error-free and accurate.
- Subsystem failures are independent; battery, propulsion and sensor failures do not interact.
- Only payload sensors can fail: flight control and navigation sensors stay functional.
- Time is discretized into fixed steps, with monitoring and evaluation performed after each step.
- The FSM contains only three modes (search, track, escape), and all mode transitions succeed.
- Predictive margin calculations are simplified to linear extrapolation based on historical data.
- Once perception conditions are met, fire sources are perfectly identified, with no missed detections or delays.

The monitored variables thus include the environmental temperature field, which is updated in each simulation step according to the fire propagation rules; thrust and power demand, which are calculated based on engine performance at the current environmental temperature and airspeed; battery temperature and SOC, which are driven by instantaneous load and recorded for slope smoothing and predictive estimation; and sensor health, which is a probability value accumulated over time.

In terms of forward-looking margin estimation, during the tracking phase, the system performs margin estimation at each time step after a warm-up period of 10 seconds. The minimum evacuation time $t_{complete-min}$ is estimated by multiplying the grid distance from the current location to the nearest boundary by Δt. Battery overheating time $t_{overheat}$ is estimated using a smoothed slope $\overline{dT/dt}$ of the most recent window of the temperature sequence T_{batt}:

$$t_{overheat} = \begin{cases} 0, & T_{batt} \geq T_{soft} \\ \infty, & \overline{dT/dt} \leq 0 \\ \frac{T_{soft} - T_{batt}}{\overline{dT/dt}}, & \text{otherwise} \end{cases} \tag{25}$$

Low-SOC time is estimated as the remaining time until reaching SOC_{min}, based on the smoothed current $\bar{I}$:

$$t_{soc} = \frac{C_{remain} - SOC_{min} C_{max}}{\bar{I}} \times 3600 \tag{26}$$

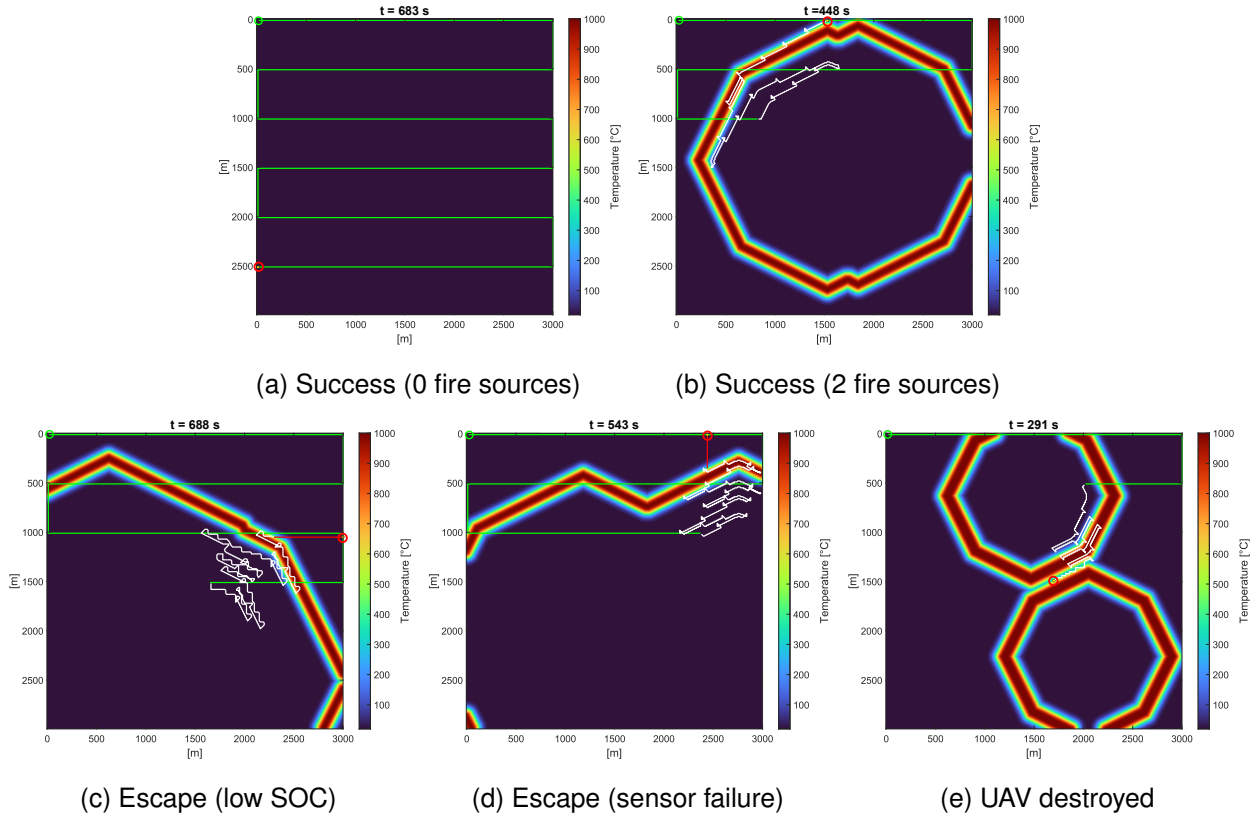
If $t_{track} \geq t_{warmup}$ and $t_{complete,min} > s \cdot \min(t_{overheat}, t_{soc})$, the system determines that the remaining margin is insufficient and switches to escape mode (s is a safety margin factor).This mechanism unifies environmental thermal loads, dynamic reachability, and electrochemical depletion into a single time-domain metric, enabling direct monitoring of the health status of the subsystems.

4. Results & Discussion

4.1 Mission Outcomes

300 simulations were run, and results were analysed to evaluate the robustness and effectiveness of the system across different fire scenarios. Examples of simulation results are shown in Fig. 6, which includes both successful missions, and missions ending in UAV escape or destruction. The plots capture fire conditions at the final time step (corresponding to mission completion), together with the UAV's full flight trajectory. The green, white and red lines indicate the flight path during *search mode*, fire line *tracking mode*, and *escape mode*, respectively.

Subfig. 6a shows the baseline case of an area search with no fire occurring, while subfig. 6b illustrates a simulation run resulting in successful mission outcome (outcome=1), starting with two random fire sources. A more complete view of the latter test is given in Fig. 7, which shows snapshots taken at different times during the simulation. As can be seen, the UAV initially conducts an area search following a lawnmower pattern. Upon detecting a fire, it switches to fire line tracking mode, continuing until it follows the fire line to the map boundary, at which point the mission ends. If no fire is detected



(a) Success (0 fire sources) (b) Success (2 fire sources)

(c) Escape (low SOC) (d) Escape (sensor failure) (e) UAV destroyed

Figure 6 – Example of simulation results for different fire scenarios. Plots show the instant before the simulation run ends: paths (green: search mode; white: track mode; red: escape mode) are overlaid on fire-temperature maps.

throughout, the UAV continues its search until reaching the map boundary. As the number of fire sources increases, the UAV trajectories become more complex, however the system remains capable of achieving global coverage and ensuring information acquisition.

Subfigures 6c–6e show unsuccessful mission examples. Once again, the UAV starts by performing a search and tracking the fireline once detected. However, at some point during the tracking, the escape mode is triggered, due to a sensor failure, a low SOC, or thermal runaway. In the first two cases, the UAV is able to reach the map boundary and make a successful escape. The time evolution of the low-SOC example is shown in Fig. 8. In the last example, fig. 6e, a more severe issue occurs (thermal runaway), which leads to destruction of the UAV before it can reach the map boundary.

Table 3 shows the distribution of mission outcomes across all 300 simulations, classifying these according to the final UAV state and the type of triggering event. The UAV successfully completed its mission in 67% of runs, showing that the framework's enables effective search and tracking missions in unknown environments. Within the successful runs, outcome "0" (early withdrawal based on safety margin prediction) occurred 5.3% of times, reflecting the system's ability to predict changes in its own health status. This functionality allows the UAV to switch mission modes before reaching dangerous thresholds, thus ensuring safety. 29.3% of results led to an escape outcome: these cases included sensor failure (ID 2) and low battery (ID 4), while battery overheating (ID=3) never led to successful escape. These results show the system can promptly perceive risks during task execution and maximise aircraft safety by executing a successful escape. The proportion of failure mission outcomes was 3.0% (ID 5, UAV destruction due to battery thermal runaway), meaning that the UAV was able to maintain its own safety (i.e. avoid catastrophic failures) in 97% of runs.

The behaviours illustrated in the discussed examples all align with the intended behaviours outlined in Sec. 2.. The simulations results demonstrate that the reconfigurable mission planning system possesses strong task completion capability and protective effectiveness in high-risk environments.

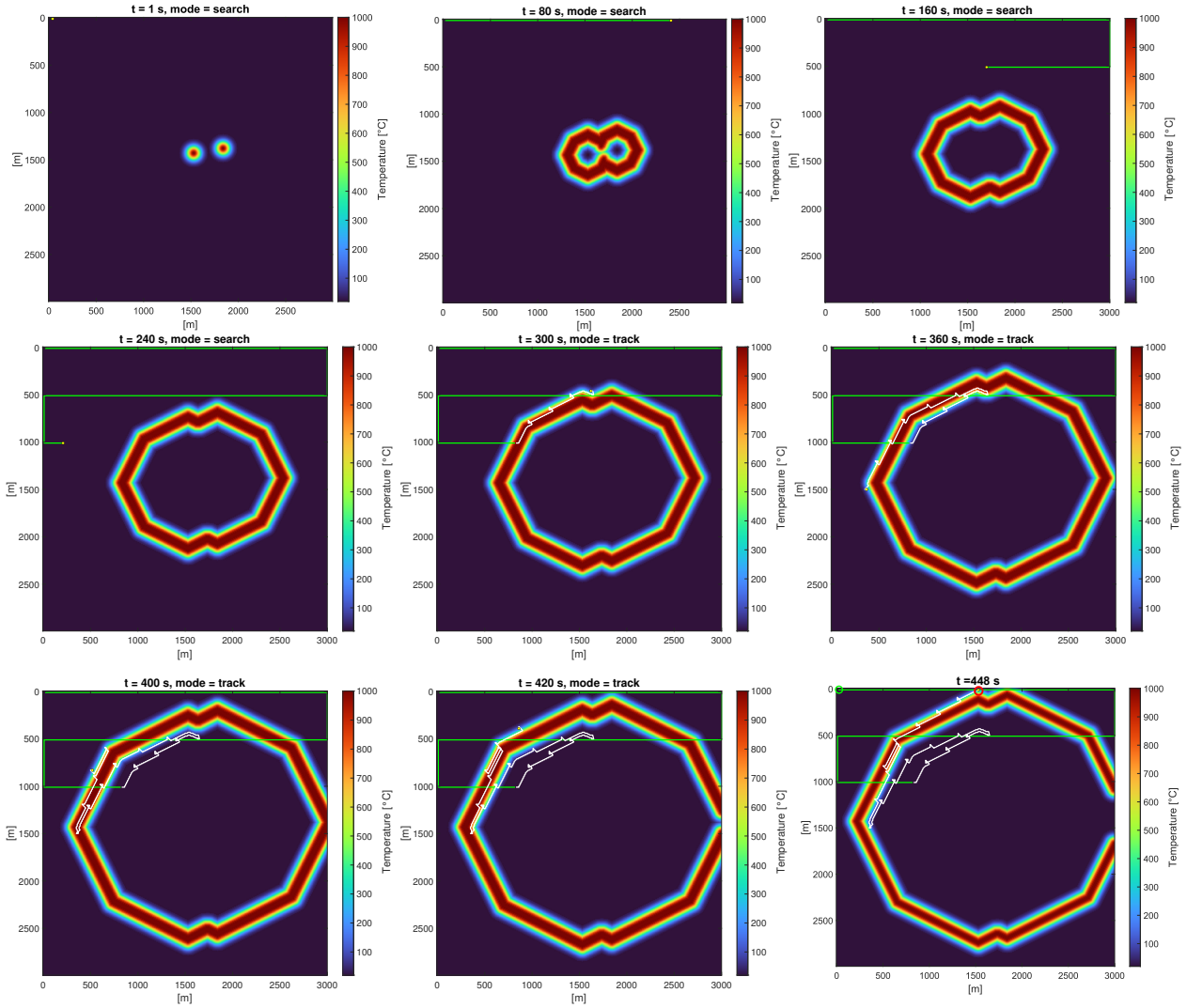


Figure 7 – Example of time evolution of a mission (successful completion, 2 fire sources).

Outcome ID	Outcome	Outcome description	Count	Percentage
0	Success	Early withdrawal driven by margin estimation	16	5.3%
1	Success	Mission completed without any damage	187	62.3%
2	Escape	Sensor failure	82	27.3%
3	Escape	Battery overheating	0	0%
4	Escape	Low battery	6	2.0%
5	Destroyed	Battery thermal runaway	9	3.0%

Table 3 – Statistical distribution of simulation mission outcomes.

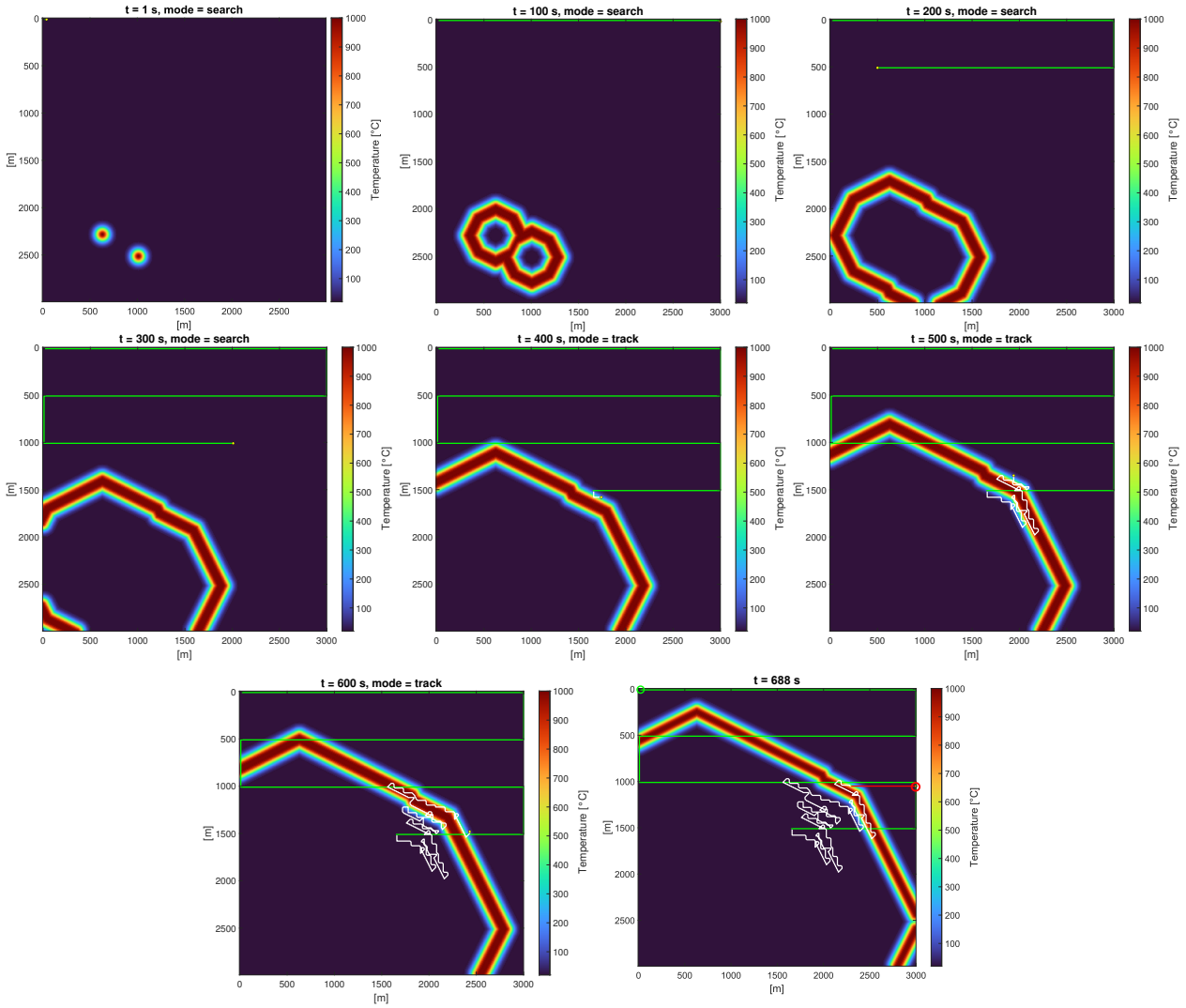
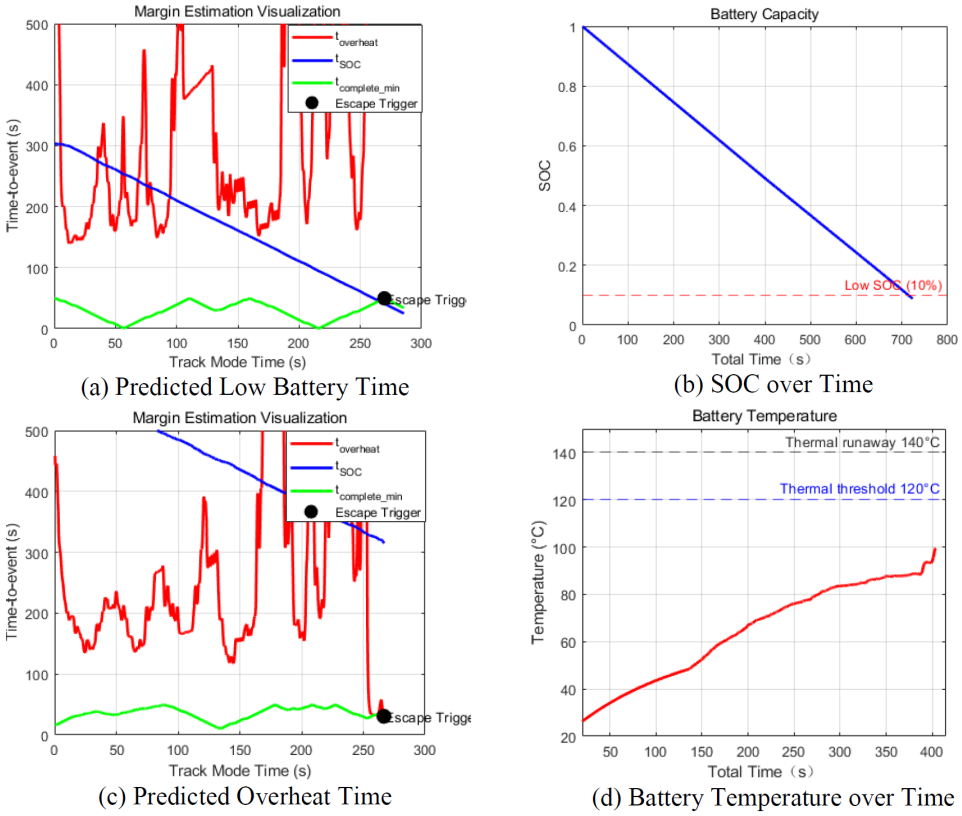


Figure 8 – Example of time evolution of a mission (escape due to low SOC, 2 fire sources).



(a) Predicted Low Battery Time (b) SOC over Time

(c) Predicted Overheat Time (d) Battery Temperature over Time

Figure 9 – Forward margin analysis results

4.2 System Performance Metrics

Further analyses were conducted to assess the system's performance beyond mere mission outcome. To evaluate how predictive safety metrics help the UAV anticipate critical failures and trigger escape manoeuvres, a forward margin analysis was conducted. Two instances of battery capacity and thermal safety margin triggers are discussed here as representative examples. Figure 9(a) illustrates the predicted time to energy depletion (t_{SOC}) and track mode completion time ($t_{complete}$) as the mission evolves. As the mission progresses, t_{SOC} steadily decreases until intersecting with $t_{complete}$. This intersection point marks the predicted moment when the UAV will become unable to complete the mission due to insufficient energy availability, and is therefore designated as the critical threshold for triggering an escape manoeuvre. Fig. 9(b) further illustrates the trajectory of SOC with increasing mission duration. In this instance, the margin-based prediction triggered an escape manoeuvre at approximately 690 seconds, before the actual battery depletion time at 710 seconds. This shows that the proactive margin mechanism enables the system to anticipate critical energy shortages, initiating a controlled withdrawal before the battery reaches critically low levels.

An analogous analysis was conducted for the thermal safety margin. Fig. 9(c) plots predicted overheat time ($t_{overheat}$) versus task completion time, with the intersection point similarly defined as the escape trigger moment. The corresponding battery temperature over time is shown in subfig. (d). As can be seen, once the system detected an abnormal sudden temperature rise, the margin calculation prompted an escape manoeuvre before the thermal threshold was reached. Battery temperature thus remained below the safety threshold throughout the mission, again showing the protective role of forward margin estimation in maintaining long-term battery health.

Fig. 10 plots information value against tracking duration. The blue data points represent simulation data and the red curve is a fitted linear regression line. The strong linear relationship indicates that the UAV can continuously accumulate information during tracking mode, with the final information value being nearly proportional to tracking duration. This showcases the planner's adaptability in dynamic environments. A linear information acquisition process is also highly predictable, enabling mission planners to estimate the total information obtainable based on mission duration.

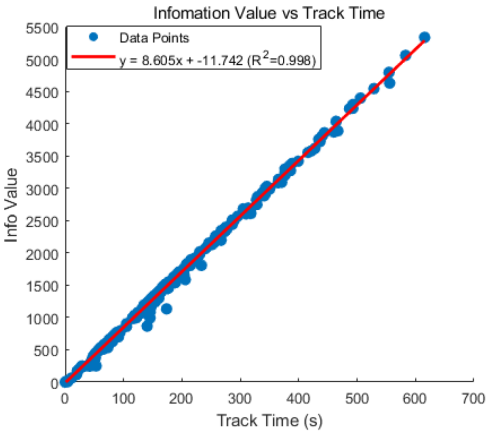


Figure 10 – Information value as a function of track time

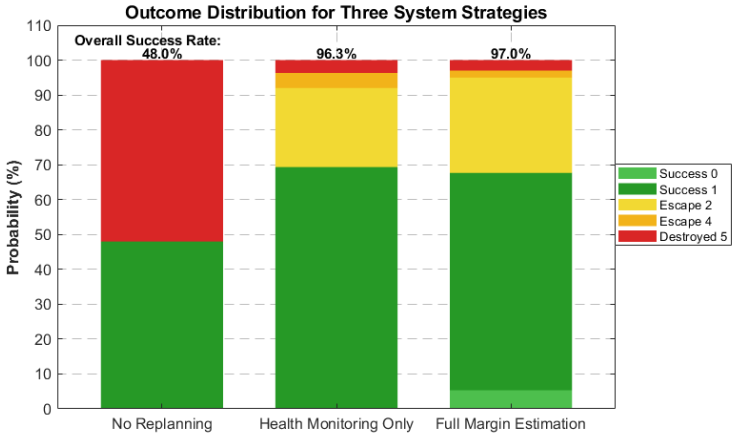


Figure 11 – Comparative outcome probabilities for the three main system trategies

4.3 System Strategy Comparison and Analysis

To verify the independent contributions of each module in the proposed architecture, further tests were conducted comparing three setups: (1) basic path planner without replanning mechanism; (2) path planner with real-time system health monitoring, but without forward margin estimation (i.e. system only responds passively to faults); (3) complete solution proposed, including health monitoring, forward margin estimation and reconfigurable planner. These three strategies were each run 200, 300, and 300 simulations respectively. The statistical results of the outcomes are shown in Figure 11. The results reveal fundamental differences in performance and safety between the strategies. The performance of strategy (1) clearly demonstrates the need for introducing the proposed reconfigurable mission planning capability. The resulting failure rate (“Destroyed 5”) of approximately 52.0% shows that simple static path planning is unable to cope with uncertainty or with performance degradation. Strategy (2) achieved a significantly better performance, with a mission success rate (“Success 1”) of 69.3% and an overall success rate (avoiding destruction, i.e. “Success 0”+“Success 1”) of 96.3% – demonstrating that the ability to respond to faults and trigger safety procedures substantially increases the likelihood of both UAV survival and successful mission completion. However, after introducing forward margin estimation in strategy (3), a more intelligent decision-making behaviour emerged. Compared with strategy (2), the overall mission success rate (“Success 0”+“Success 1”) was slightly lower, at 67.7%, however the occurrence of "low battery escape" (“Escape 4”) and "destruction" (“Destroyed 5”) outcomes decreased, respectively, from 4.3% to 2.0% and from 3.7% to 3.0%. This highlights a key advantage of the proposed algorithm. It does not aim merely to increase the mission success rate, but rather to achieve the optimal balance of safety and mission success.

5. Conclusions

This research proposes a dynamic reconfigurable mission planning framework, which integrates real-time perception, forward margin estimation, and multi-modal decision-making mechanisms to achieve a collective optimization of performance and safety for UAVs in wildfire monitoring missions. Simulation experiments show that the proposed method significantly enhances the adaptability, survivability, and mission efficiency of the system. Through dynamic risk assessment and forward-looking decision-making, the system can actively trigger mission reconfiguration. When facing potential or actual faults, it can perform corresponding safe operations, thereby ensuring the mission success rate and the platform security. This study lays the foundation for reconfigurable UAV mission planning in dynamic environments. Future work will extend the decision-making capability of the framework to enable the system to learn optimal risk trade-off strategies for different task stages. More comprehensive evaluations will be performed, first by incorporating more realistic temperature field and sensor models in the simulation, and ultimately via hardware-in-the-loop experiments and flight tests.

6. Contact Author Email Address

s.armanini@imperial.ac.uk

7. Copyright Statement

The authors confirm that they hold copyright on all of the original material included in this paper. The authors confirm that they give permission for the publication and distribution of this paper as part of the ICAS proceedings or as individual off-prints from the proceedings.

References

[1] R. Bailon-Ruiz, A. Bit-Monnot, and S. Lacroix. Planning to monitor wildfires with a fleet of UAVs. In *IEEE/RSJ Int Conf Intell Robots and Systems (IROS)*, 2018.

[2] Y. Wu, J Gou, H Ji, and J Deng. Hierarchical mission replanning for multiple uav formations performing tasks in dynamic situation. *Computer Communications*, 200, 2023.

[3] H. Usach and J. A. Vila. Reconfigurable mission plans for rpas. *Aerosp. Sci. Technol.*, 96, 2019.

[4] P. Shobeiry, M Xin, X Hu, and H Chao. UAV path planning for wildfire tracking using partially observable markov decision process. In *AIAA Scitech Forum*, 2021.

[5] G. A. Hollinger and G. S. Sukhatme. Sampling-based robotic information gathering algorithms. *The International Journal of Robotics Research*, 33(9), 2014.

[6] X. Zhao, M Osborne, J Lantair, V Robu, D Flynn, X Huang, M Fisher, F Papacchini, and A Ferrando. Towards integrating formal verification of autonomous robots with battery prognostics and health management. In *Lecture Notes in Computer Science*, volume 11724. Springer, 2019.

[7] K. Almazrouei, I. Kamel, and T. Rabie. Dynamic obstacle avoidance and path planning through reinforcement learning. *Applied Sciences*, 13(14), 2023.

[8] M. Popovic, T Vidal-Calleja, G Hitz, JJ Chung, I Sa, R Siegwart, and J Nieto. An informative path planning framework for uav-based terrain monitoring. *Auton. Robots*, 44(6), 2020.

[9] B. J. Julian, M Angermann, M Schwager, and D Rus. Distributed robotic sensor networks: An information-theoretic approach. *Int. J. Robotics Research*, 31(10), 2012.

[10] M. Mehta, C. Kulkarni, M. Khasin, and J. Lawson. Predicting thermal response in a li-ion cell on a uav flight profile. Presentation, NASA Ames Research Center, 2022. Online; accessed Aug. 31, 2025.

[11] A.D. Gordon, A. El-Suleiman, R.E. Donatus, M.U. Bonet, and S.D. Iyaghigba. Aerodynamic analysis of a conceptual fixed-wing vertical take-off and landing uav powered by a piston engine. *Journal of Science Technology and Education*, 13, 2025.

[12] Manh-Kien Tran, Anosh Mevawalla, Attar Aziz, Satyam Panchal, Yi Xie, and Michael Fowler. A review of lithium-ion battery thermal runaway modeling and diagnosis approaches. *Processes*, 10(6), 2022.

[13] Dwijendra Dubey, A. Mishra, Subrata Ghosh, M.V. Reddy, and Ramesh Pandey. Geometry-influenced cooling performance of lithium-ion battery. *Applied Thermal Engineering*, 230:120723, 2023.

[14] E. Petritoli, Leccese F., and L. Ciani. Reliability and maintenance analysis of unmanned aerial vehicles. *Sensors*, 18(9), 2018.

[15] L. Shu, M. Wang, X. Tian, X. Zhang, and X. Dai. Calculation and description of forest fire behavior characters. *Scientia Silvae Sinicae*, 40(3):179–183, 2004.

[16] Y. Yu et al. A method for two-dimensional temperature distribution reconstruction using compactly supported and gaussian radial basis function. In *International Congress on Advanced Applied Informatics (IIAI-AAI)*, pages 1083–, 2019.

[17] W. Mell et al. A physics-based approach to modelling grassland fires. *International Journal of Wildland Fire*, 16(1), 2007.

[18] P. E. Dennison et al. Wildfire temperature and land cover modeling using hyperspectral data. *Remote Sensing of Environment*, 100(2):212–, 2006.